The XFM beamline at the Australian Synchrotron

Daryl L. Howard, Martin D. de Jonge, Nader Afshar, Chris G. Ryan, Robin Kirkham, Juliane Reinhardt, Cameron M. Kewish, Jonathan McKinlay, Adam Walsh, Jim Divitcos, Noel Basten, Luke Adamson, Tom Fiala, Letizia Sammut and David J. Paterson

IUCr Journals
CRYSTALLOGRAPHY JOURNALS ONLINE

The XFM beamline at the Australian Synchrotron

Daryl L. Howard,[a]* Martin D. de Jonge,[a] Nader Afshar,[a] Chris G. Ryan,[b] Robin Kirkham,[b] Juliane Reinhardt,[c] Cameron M. Kewish,[a,d] Jonathan McKinlay,[a] Adam Walsh,[a] Jim Divitcos,[a] Noel Basten,[a] Luke Adamson,[a] Tom Fiala,[a] Letizia Sammut[a] and David J. Paterson[a]*

[a]Australian Synchrotron, ANSTO, 800 Blackburn Road, Clayton, Victoria 3168, Australia, [b]Commonwealth Scientific and Industrial Research Organisation, Normanby Road, Clayton, Victoria, Australia, [c]Advanced Light Source, Lawrence Berkeley National Laboratory, 1 Cyclotron Road, Berkeley, CA 94720, USA, and [d]Department of Chemistry and Physics, La Trobe Institute for Molecular Science, La Trobe University, Australia.
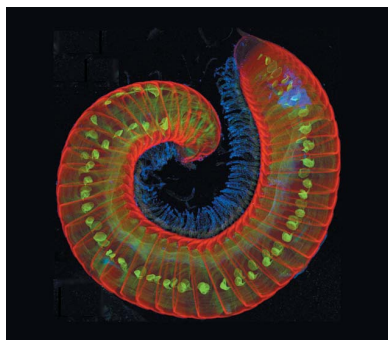*Correspondence e-mail: darylh@ansto.gov.au, davidp@ansto.gov.au

The X-ray fluorescence microscopy (XFM) beamline is an in-vacuum undulator-based X-ray fluorescence (XRF) microprobe beamline at the 3 GeV Australian Synchrotron. The beamline delivers hard X-rays in the 4–27 keV energy range, permitting K emission to Cd and L and M emission for all other heavier elements. With a practical low-energy detection cut-off of approximately 1.5 keV, low-Z detection is constrained to Si, with Al detectable under favourable circumstances. The beamline has two scanning stations: a Kirkpatrick–Baez mirror microprobe, which produces a focal spot of 2 μm × 2 μm FWHM, and a large-area scanning 'milliprobe', which has the beam size defined by slits. Energy-dispersive detector systems include the Maia 384, Vortex-EM and Vortex-ME3 for XRF measurement, and the EIGER2 X 1 Mpixel array detector for scanning X-ray diffraction microscopy measurements. The beamline uses event-mode data acquisition that eliminates detector system time overheads, and motion control overheads are significantly reduced through the application of an efficient raster scanning algorithm. The minimal overheads, in conjunction with short dwell times per pixel, have allowed XFM to establish techniques such as full spectroscopic XANES fluorescence imaging, XRF tomography, fly scanning ptychography and high-definition XRF imaging over large areas. XFM provides diverse analysis capabilities in the fields of medicine, biology, geology, materials science and cultural heritage. This paper discusses the beamline status, scientific showcases and future upgrades.

1. Introduction

X-ray Fluorescence Microscopy (XFM) is a hard X-ray beamline at the Australian Synchrotron (Boldeman & Einfeld, 2004) which has enjoyed user operations for the past decade and specializes in the spatially resolved detection of elements at the micrometre length scale, XANES imaging, and large-area elemental mapping. There have been significant revisions to the beamline since the last beamline paper was published early in its operation (Paterson *et al.*, 2011), thus compelling a new overview. A summary of the XFM hardware and parameters are presented in Table 1.

X-ray fluorescence (XRF) methods have several favourable characteristics for elemental detection. Specimens can typically be analysed non-destructively and quickly with minimal or no sample pre-treatment, and simultaneous detection of many elements in a single measurement with high sensitivity is possible. XRF combined with a micro-focused beam in a sample scanning arrangement is a potent tool for highly resolved elemental detection. XFM utilizes a Kirkpatrick–

beamlines

Beamline name	X-ray Fluorescence Microscopy – XFM
Source type	In-vacuum undulator (90 periods of 22 mm length)
Monochromation	Double-crystal Si(111) or Si(311), liquid N_2 cooled
Energy resolution, $\Delta E/E$	$\sim 3.1 \times 10^{-4}$ (see Appendix A)
Energy range	4–27 keV
Photon flux† (photons s^{-1})	
7 keV	10^{11}
10.0 keV	2×10^{10}
12.9 keV	2×10^{10}
15.8 keV	8×10^{9}
18.5 keV	4×10^{9}
27 keV	$\leq 10^{9}$
Beam spot size	
Milliprobe	≥ 100 µm
KB microprobe	IDT small KB, 2×2 µm
Confocal optic	XOS, 2.5 mm input focal distance
Fluorescence detectors	Maia 384 C (275 eV)‡ (milliprobe)
	Maia 384D (275 eV)‡ (microprobe)
	Hitachi Vortex EM, FalconX (155 eV)‡
	Hitachi Vortex ME3, FalconX (135 eV)‡
Pixel array detector	Dectris EIGER2 X 1M
Ion chambers	Oken S-1194A1
Current preamplifiers	Stanford Research SR570
Cryogenic capability	Oxford Cryostream 700 Series

† The energies listed from 10 to 18.5 keV are most commonly used for mapping on XFM. ‡ Energy resolution FWHM Mn $K\alpha$, peaking time = 2 µs.

Baez (KB) focusing mirror microprobe for the majority of experiments, and it provides a 2×2 µm FWHM focal spot size. The Fresnel zone plate nanoprobe (Paterson *et al.*, 2011) has been decommissioned and is no longer available for user operations.

XFM has a diverse user base. Based on the past five years of merit research proposals, the percentage of activity in the following fields of research are: earth sciences (27%), biological sciences (18%), environmental sciences (12%), chemical sciences (11%), medical sciences (9%), physical sciences (6%) and engineering (6%), with the remaining 11% taken up by (nano)technology, agriculture and cultural heritage studies.

The beamline was an early adopter of the Maia energy-dispersive detector array and accompanying event-mode detection (Ryan *et al.*, 2018). Event-mode data collection significantly reduces scan time (detector readout) overheads, thus permitting rapid high-definition elemental mapping over large areas, or 3D measurements such as full spectroscopic XANES imaging (~ 100 energies) (Etschmann *et al.*, 2014; Monico *et al.*, 2015) or XRF tomography in reasonable time-frames (McColl *et al.*, 2012). These topics, the beamline status and future upgrades are discussed further in this paper. We hope this is beneficial to both prospective and experienced users of the beamline.

2. Controls

Low-level hardware control is achieved with the *Experimental Physics and Industrial Control System* (*EPICS*, http://www.aps. anl.gov/epics/) with the *Motif Editor and Display Manager* (*MEDM*, https://epics.anl.gov/extensions/medm/index.php) or *qeGUI* (https://qtepics.github.io/) graphical user interfaces. Measurement orchestration is performed from the command line using the IDL development environment (L3Harris Geospatial). Plans are underway to migrate the scan code to Python.

One of the beamline's goals is to simplify the user experience as much as possible. Scan setup on XFM is accomplished by prefilling an *Excel* spreadsheet with sample *XYZ* position coordinates, pixel size and scanning-stage velocity (which defines the pixel transit or dwell time). Rotation angles for tomography or energies for XANES are set in the IDL development environment. Individual scan times and total batch times are estimated within the spreadsheet to provide pre-launch feedback to the user. Scan control software reads the spreadsheet and sets the beamline to perform the requested scan(s) with various control keywords from the command line, *e.g.* 2D mapping (default), XANES mapping *etc*. Every measurement outlined in this article was acquired using this approach. Multiple scans can be placed in a batch and scanned sequentially; batches set for over 48 h of continuous scanning without user intervention are not uncommon. The scan software can automatically tune the sensitivity on the ion chamber preamplifiers (Stanford Research SR570) to achieve an acceptable current range before each scan launches. This is especially useful when running a batch of scans requiring different flux conditions.

The beamline also runs an 'autoshutter' script to monitor for storage-ring beam dumps. If a beam dump occurs, the script will pause a scan at the end of a scan line. Once the beam is restored to the beamline, the autoshutter script will open the front-end shutter and resume the scan after a preset warm up period (~ 30 s). The autoshutter script runs without user intervention, and enables users to leave the beamline to operate unattended for long periods of time without risk of beam time loss.

Elemental concentration standards acquisition is fully automated using the control script, once the user has changed the sample mount over to a dedicated standards mount. The script selects only those specimens with absorption edges that are below the beamline energy. Once the *XYZ* scanning stages have moved to the relevant foil, the secondary source aperture (SSA) width is adjusted to ensure correct count rate conditions on the fluorescence detectors that are in use. Following this, the current amplifier gain settings are automatically tuned, and the measurement is commenced. Standards acquisition takes around 15 min and is typically performed at least daily during an experiment (Donner *et al.*, 2013).

3. Source and beam optics

The XFM beamline optical layout is shown in Fig. 1(*a*). The insertion device is a 2 m room temperature in-vacuum undulator (IVU) with a 22 mm period (NeoMAX, Japan). Instrument Design Technology Ltd, England, performed the original build of the beamline and the KB mirror system. The beamline optical design has been discussed previously (Paterson *et al.*, 2011), but for completeness it will be briefly outlined here. The
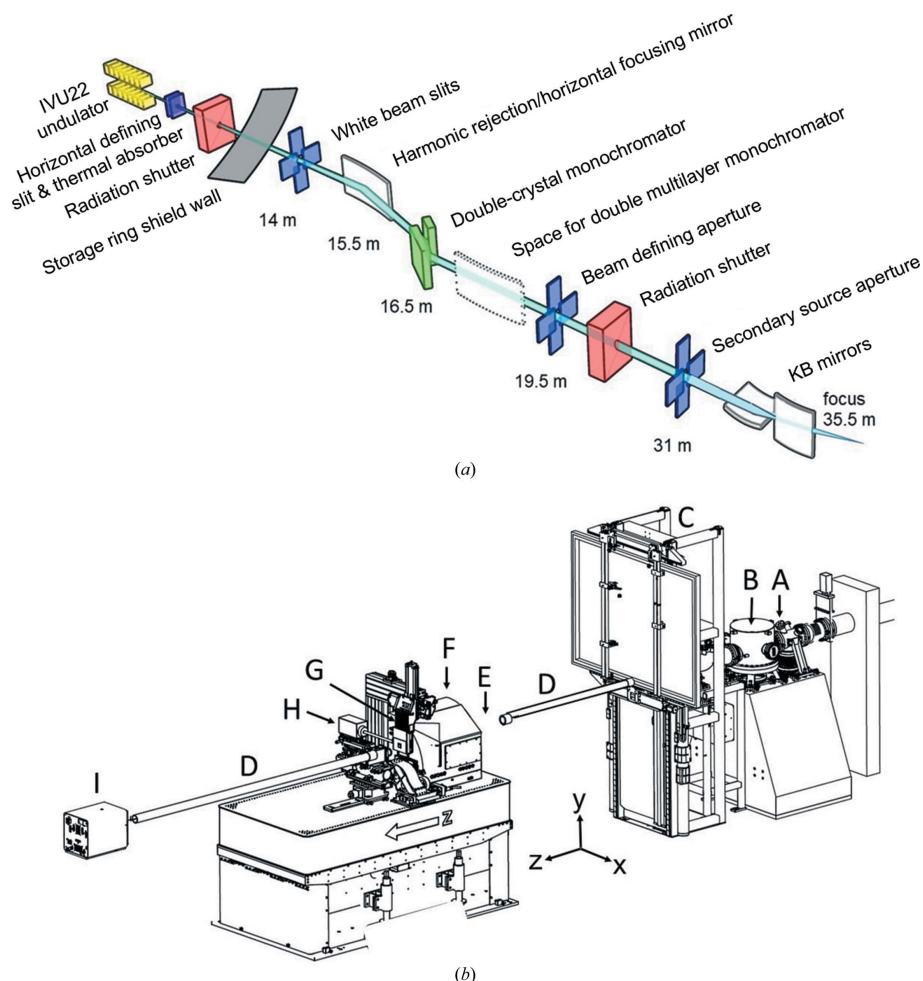
Figure 1
(*a*) A schematic layout of the XFM beamline optics. Distances are in metres from the source. (*b*) The layout of the XFM beamline experimental endstation. A = quad diode BPM, B = SSA slits (31 m from source), C = milliprobe (with painting installed, 1.5 m from SSA), D = removable helium flight tube, E = clean-up slits and ion chamber (not shown for clarity), F = KB mirror enclosure (KB focus 4.5 m from SSA), G = Maia detector, H = SDD detector and I = Eiger detector (4 m from KB focus).

geometry results in some loss of diffraction efficiency relative to the traditional vertical diffraction geometry, the loss is mitigated by the narrow acceptance angle of the microprobe optics (Paterson *et al.*, 2007; Lai *et al.*, 2007). The instrument energy resolution ($\Delta E/E$) using the Si(111) crystals is $\sim 3.1 \times 10^{-4}$ (see Appendix *A*).

Beam focus is done with a pair of KB mirrors which routinely achieve 2 μm × 2 μm FWHM spot size and have demonstrated <1 μm FWHM focal spot in high coherence (reduced flux) operations. The KB mirror shape is dynamically figured by applying two adjustable moments to a trapezoidal-shaped mirror (Eng *et al.*, 1998). The radius of curvature and ellipticity of the mirrors can be controlled independently. The mirrors operate at a grazing-incidence reflection angle of 3 mrad. Both the horizontal and vertical mirrors are manufactured from silicon and have platinum and rhodium stripes for accessing different energy ranges: Si (4–10 keV), Rh (4–22.7 keV) and Pt (>22.7 keV).

4. Endstation design and hardware

A diagram of the XFM endstation is shown in Fig. 1(*b*), which indicates the major components. An in-vacuum quadruple diode beam-position monitor (QBPM) is incorporated into a PID-controlled feedback system to maintain the position and intensity of the beam delivered to the SSA. Various ultrathin foils (Lebow) are selectable (Ti, Cr, Ni, Cu) on a rotary stage to provide a feedback signal for the QBPM. The feedback system adjusts piezo motors on the DCM second crystal pitch, DCM second crystal roll and HFM angle to maintain the desired beam intensity and position. The PIDs work at a 10 Hz rate. While the QBPM is sampled at 1500 Hz, and a fast-mode PID can be implemented, we have found a slower PID is more stable for our operations. Currently, the slow PID is in use with slew/rate control of 10 V s^{-1} (full scale per second). A scintillator screen is also selectable on the QBPM rotary stage for beam visualization at up to 100 Hz frame rate via a gigabit ethernet camera. This high frame rate is extremely useful to diagnose AC supply frequency (50 Hz in Australia) drifts.

The SSA is a stable motorized slit with polished tungsten rods as slit blades. It is approximately 0.5 m downstream of the QBPM and its horizontal aperture size is adjusted to control the amount of light delivered to the endstation. SSA openings typically range from 5 to 80 μm (H) × 200 μm (V). The

beamline uses a horizontal reflection and diffraction optical scheme similar to that proposed by Lai *et al.* (2007). It comprises a horizontal focusing mirror (HFM) and a double-crystal monochromator (DCM) in a horizontal diffraction arrangement. The HFM is made of silicon and can be translated to rhodium, platinum and silicon (bare) stripes to enable different energy ranges while suppressing higher-order harmonics. The HFM operates at a reflection angle of 3 mrad, and it is used to focus the source to the SSA in a horizontal focusing mode with demagnification of approximately 1. The vertical beam is unfocused. The horizontal diffraction of the DCM enables the horizontal apertures within the beamline to filter out any horizontal vibration and optical surface slope errors without significant intensity variations. The DCM has interchangeable liquid-nitrogen-cooled Si(111) and Si(311) crystal pairs, with Si(111) used most of the time. The DCM has demonstrated excellent stability and reproducibility during constant-energy XRF mapping and variable-energy XANES scans (Paterson *et al.*, 2011). While the horizontal diffraction

vertical size is usually kept at 200 μm to avoid creating a new source point in the vertical, but the vertical aperture size is occasionally reduced for highly concentrated samples (*i.e.* geological) to allow finer flux control. A beryllium window is located 1 m downstream from the SSA, and the remainder of the beamline is at atmospheric pressure. To reduce air scattering and absorption losses of the beam, helium-purged flight tubes are used during KB microprobe operation [Fig. 1(*b*)]. The PVC plastic flight tubes are easily removed and attached with 3D-printed KF-40 flanges. The helium from the flight tubes also purges the KB mirror enclosure.

A custom-designed scanning station known as the milliprobe has been installed to enable the analysis of large objects such as paintings (Divitcos *et al.*, 2017). The new apparatus replaces a portable set of scanning stages that were used on the KB microprobe to scan works such as a painting by Edgar Degas (Thurrowgood *et al.*, 2016). The new milliprobe can scan objects having a mass up to 15 kg over an area 600 mm × 1100 mm (Parker 404XR and 406XR stages with Parker SM232BE servo motors) up to a maximum speed of 175 mm s^{-1}, with 40–60 mm s^{-1} being typical. The vertical 406XR stage has a shaft brake in case of power loss. The milliprobe is designed for the ready mounting of rectangular specimens, but complex objects such as fossils and artefacts can be analysed with custom mounting attachments. The time required to mount a painting is several minutes. The beam size for the milliprobe is defined by the SSA slits, which are 1.5 m upstream from the sample plane, and the finest resolution is approximately 100 μm due to the beam divergence of the SSA. Flattening of the HFM could reduce this beam divergence for higher resolution, but to date this has not been required. A nitrogen-filled ion chamber (Oken S-1194A1) is positioned upstream of the milliprobe to measure the incident flux. A radiation shutter (Thorlabs SH1 with SC10 controller) is also upstream of the milliprobe, which automatically opens and closes at the beginning and end of a scan, respectively, to minimize radiation dose to the sample. An Australian five cent coin (75% Cu, 25% Ni, 1.3 mm thick) is epoxied to the original Al shutter to effectively block the incident hard X-ray beam, and its low mass (2.8 g) does not hinder the shutter's actuation. Portions of the milliprobe that can potentially enter the beam path, such as support struts and specimen hard stops, are constructed of carbon fibre; their high X-ray transmissivity, low fluorescence yield, low weight and high stiffness are beneficial properties.

The KB mirror microprobe is the workhorse apparatus of XFM. Like the milliprobe, it has an identical automatically actuating radiation shutter and an upstream nitrogen-filled ion chamber to measure incident flux, which doubles as the transmission detector for the milliprobe if it is in operation. A set of beam-defining or beam clean-up slits (CUS) is located immediately upstream of the ion chamber. The majority of samples are affixed with double-sided adhesive tape to a flat Perspex mount that has apertures to transmit the beam. Various mount designs are available to accommodate the diverse sample types and sizes. The mount is attached to the sample *XYZ* (horizontal, vertical, beam axis) scanning stages

(Parker models MX80L, MX80, 808004CT) in a matter of seconds with a Newport M-BK-3A magnetic kinematic base and plate arrangement. The resolution of the *X* and *Y* stages is 20 nm and of the *Z* stage is 100 nm, and the encoders are mounted on the stages. The *X* axis is capable of 200 mm s^{-1}, but is usually limited to 20 mm s^{-1}, while the minimum speed is ≥0.02 mm s^{-1} for reliability. The scanning area is approximately 140 mm × 98 mm (H × V). A set of beam-defining apertures (BDA), pinholes (Ted Pella, Mo or Pt:Ir 95%:5%, 0.25 mm thick) of various diameters in the range 75–500 μm to reduce beam scatter tails from the KB mirrors, are on an *XY* motor stack immediately downstream of the KB mirror enclosure.

A sample transmission ion chamber is on an *XYZ* stack directly downstream of the sample scanning stages. To reduce the collection of air scatter back into the Maia detector, a polyether ether ketone (PEEK) snout with adjustable length is affixed to the upstream end of the ion chamber. The snout performs best when placed close to the rear of the sample; its aperture is approximately 1 mm.

Scanning motion 'overheads' can be a significant waste of beam time. Excessive end-of-line overheads were detrimental to 3D scanning modes such as XANES imaging and XRF tomography where in some instances the overheads could account for 50% of the total scan time. To minimize these overheads, an efficient raster scanning control system, *RASCAN*, was programmed into a Delta Tau GeoBrick LV motion controller (Afshar *et al.*, 2017). *RASCAN* incorporates a parabolic (kinematically optimized) trajectory that minimizes end-of-line turnaround, significantly reducing scan time overheads. In this scanning mode, the horizontal (fast axis) is in continuous motion, following a serpentine or boustrophedon path. In KB microprobe operation, the line overhead time is velocity dependent and has improved from approximately 350 ms to 45 ms with the addition of *RASCAN*. Before *RASCAN*, the daily overheads were 1–4 h, which reduced to 10–30 min after its implementation. The improved raster scanning algorithm has significantly mitigated potential radiation damage to sensitive samples such as fresh plants (Blamey *et al.*, 2018).

Two main types of scanning mode are used on XFM in which the sample is oriented at either 90° or 45° to the beam axis. The *XYZ* scanning stages scan in the orthogonal geometry for Maia detector use. For 45° scanning with an SDD located at 90° to the beam path, a 45° kinematic mount adaptor is attached to the *X* stage, and a simultaneously coordinated motion of the *XZ* motors is used to keep the sample plane in the X-ray beam focus and prevent crashing with the SDD. The coordinated motion is programmed in the motion control system. An advantage of the setup is that mechanical rearrangement of the scanning stages is not necessary when switching between orthogonal and 45° scanning modes. Progress is being made to unify these two coordinate systems so that a specimen can be measured in either geometry without needing to change the scan coordinates.

Samples are visualized on the KB microprobe with several gigabit ethernet cameras. Due to the restricted space upstream

of the sample with respect to the KB mirror enclosure and detectors, viewing is to the rear of the sample. Fiducial markers are positioned on the camera viewing software (*areaVision*, Dr Stephen Mudie) to indicate the X-ray beam position for initial sample alignment and coordinate selection. Two cameras with 5× and 10× objective lenses are on the sample transmission chamber *XYZ* stage stack downstream for higher-magnification specimen viewing. The maximum effective optical resolution corresponds to 0.35 µm per CCD camera pixel using a 10× Mitotoyo M Plan APO objective lens with about 175 mm of extension tube. This permits characterization of the ∼2 µm focal beam spot on a thin scintillator, for example.

5. XRF detectors and event-mode data acquisition

The majority of the XRF measurements on XFM are with the Maia 384-element detector array (Ryan *et al.*, 2014, 2018). The sensor is a monolithic silicon planar array of 384 1 mm × 1 mm detector elements, 0.4 mm thick, connected to 384 independent analogue channels. The central 4 mm × 4 mm of the detector have been removed to accommodate a 0.5 mm diameter aperture through which the focused beam passes onto the sample. The inter-element regions of the sensor are shielded using a three-layer molybdenum mask which collimates the light from a focus that is around 10 mm from the detector sensor, which corresponds to approximately 2.5 mm working distance from the detector body. The array uses a back-scatter annular configuration, which has a 1.3 sr solid-angle detection geometry. With this design, there is complete freedom in sample size and scanning range.

The beamline has recently purchased a three-element Hitachi Vortex ME3 silicon drift detector (SDD) to supersede a single-element Vortex. The Vortex ME3 is a custom design with the three elements arranged vertically, with the on-axis (central) element of 80 mm^2 active area, and the two off-axis elements of 50 mm^2 active area. The motivation for this particular design was to balance count rates on each sensor, as the smaller top and bottom sensors will detect more X-ray scatter than the larger central sensor, which is positioned in the X-ray scatter minimum geometry (Sun *et al.*, 2015). We hope to report on this design following implementation.

Event-mode acquisition of energy-resolved spectral data is used on XFM, where each photon event is tagged by position in a scan with the identity of the detector element recording for the event. Event mode remains relatively rare in the synchrotron environment. A key motivation for event mode is the zero detector time overheads it provides. Briefly, photon events (*nET*) contain the detector channel (*n*), X-ray energy (*E*) and time-over-threshold (*T*). The time-over-threshold is a measure of the dead time and is used with *E* for pileup rejection. The photon events enter a processing pipeline in a field programmable gate array (FPGA) in the Maia detector processor, where they are placed into an event buffer. It is possible to sub-sample or 'throttle' photon events from intense lines such as major element fluorescence or scatter to reduce downstream data rates in a restorable way (Kirkham *et*

al., 2010). In practical terms, for biological samples we find that applying a throttle to the elastic and inelastic scatter reduces the saved data volume by about a factor of four with no loss in data quality. The FPGA also integrates frequency input from upstream (I_0) and downstream (I_1) beam intensity monitors and in real time uses the stage encoder signals to derive a 'pixel address' in the scan, given an assigned origin and pixel size for each axis. Stage movement across pixel boundaries triggers output of the buffer as an *ET* record and each record is tagged by the pixel address, the acquisition time interval and integrated flux counts, without additional post-processing (Ryan *et al.*, 2014). The sample stage rotational axis or the DCM Bragg angle encoder may also be used as a pixel address in addition to the Cartesian sample position to acquire 3D tomographic or XANES data sets with complete freedom in the choice of scanning axis order.

Real-time viewing of the data is possible from the on-board processing of the FPGA using a predefined dynamic analysis (DA) matrix, giving users immediate feedback of the sample under analysis. The immediate feedback can potentially save significant experimental time as it allows real-time revision of scan parameters. The predefined matrix is often rudimentary at the beginning of analysis, but it is quickly refined to provide high-quality feedback to drive scientific enquiry.

Digital signal processing which incorporates real-time pulse pile-up recovery (Scoullar *et al.*, 2011) of the Vortex SDD data stream is handled with an XIA FalconX processor. The Vortex data are written in list mode, providing similar functionality to the Maia event mode. The list-mode function can include a wide variety of data into the output data stream: event energies (with or without time stamps), gate states and encoder values, as well as general time stamps. Each detector channel of the FalconX list-mode data stream is written to disk separately, and then merged in a pre-processing step before analysis. Currently the FalconX data stream does not have real-time analysis, but could work in principle with a client–server relationship requesting records. This would require implementation of the DA matrix/lookup table approach, either within the client, or within the server for better efficiency.

6. Sample mounting and environments

The beamline sample environment is in air, which we have found to be versatile for the wide array of sample types encountered on XFM. For studies where atmospheric argon is problematic for detection of low-energy fluorescence lines such as Ag *L* or low-*Z* trace elements, a so-called argon exclusion chamber can be attached to the Maia detector (Howard *et al.*, 2018). The chamber is a Perspex enclosure of approximately 0.3 l volume through which nitrogen is flowed at approximately 1 l min^{-1}. The chamber has a downstream window made of polyimide film to minimize scatter, and the bottom of the enclosure is partially open to allow sample access and permit raster scanning. Due to stage range limitations and space restrictions with the argon exclusion chamber, the scan range is limited to 56 mm × 30 mm (H × V).

For studies with an SDD detector, lower-energy sensitivity can be improved with a flow of nitrogen or helium through a high-purity Al collimator that is attached to the detector snout.

For sample supports, we recommend quartz slides for petrographic sections of less than 100 µm thickness, as normal glass microscope slides often have trace heavy metals that may contribute an unwanted background. For tissue and cell cultures, silicon nitride (Si_3N_4, 0.5–1 µm thick) windows are recommended (Carter *et al.*, 2010; Bissardon *et al.*, 2019).

For samples sensitive to radiation damage, a cryogenic stream environment is available (Oxford Cryostream 700 Series), where the stream is directed downwards. It typically operates at $-100°C$ and is effective in minimizing the influence of radiation damage in organisms such as *Caenorhabditis elegans* (Jones *et al.*, 2017) and hydrated plant material (Jones, Kopittke *et al.*, 2019). A jacket flow of dried facility-compressed air is used to avoid the inherent noise, vibration and bulk of a local compressor. Instead, the compressed air is processed with a membrane air dryer and mist separator (SMC IDG Series Type V). For Cryostream work, typical sample-holder options are a carbon fibre rod (50 mm long × 2 mm diameter; see XRF tomography section below), a carbon fibre stick (100 mm × 10 mm × 1 mm) that holds one rigidly mounted specimen, or one of the standard beamline Perspex sample holders with the top crosspiece removed that can be used to hold a specimen between two sheets of Ultralene (SPEX SamplePrep) 4 µm thick film (Gei *et al.*, 2018). The 20 mm diameter Cryostream consists of a 7 mm inner diameter cold jet nozzle, which is surrounded by a warmer outer jacket of air. Samples must be scanned completely within the cold jet to maintain cold temperatures, thus limiting the maximum practical sample width to approximately 2 mm. Icing is not usually a problem except on exceptionally humid days. At present we do not have a dedicated cryogenic sample-transfer system, and so most specimens are frozen *in situ* using the Cryostream cold flow. While the cooling rate using this approach is not suitable for structural preservation at the finest length scales, it is sufficient at the $\sim$1 µm length scales addressed on the XFM beamline. However, on occasion cryogenic transfer has been accomplished by using either fast human-guided transfer methods or dry-ice backed transfer. At present, these methods are suitable for our resolutions and applications.

7. Beamline techniques

7.1. 2D elemental mapping

Fast scanning XRF 2D elemental mapping at the micrometre scale is the foundation beamline mode on XFM. Depending on the sample's elemental concentration and scattering power, dwell time per pixel is usually about 1 ms, give or take an order of magnitude. Scan images up to around 100 Mpixels are common. An example scan showing the elemental morphology of a Portuguese millipede is shown in Fig. 2(*a*), measured in 2 h with 5 µm × 5 µm pixels and 1 ms dwell (5 mm s^{-1} scan velocity). The Compton (inelastic) scattering image is shown in Fig. 2(*b*), highlighting the overall morphology of the millipede. The high fidelity of the Compton image is due in part to the backscatter geometry of the Maia detector, which collects more scatter from the specimen. The Compton scatter feature has been used to demarcate the boundary of macrophage cells (James *et al.*, 2013) or image a painting's canvas under many layers of paint (Howard *et al.*, 2012).

When beginning an experiment on XFM, users will typically rapidly scan the majority, or all, of a large specimen at a relatively coarse resolution of tens to hundreds of micrometres to get a general overview of its composition. This
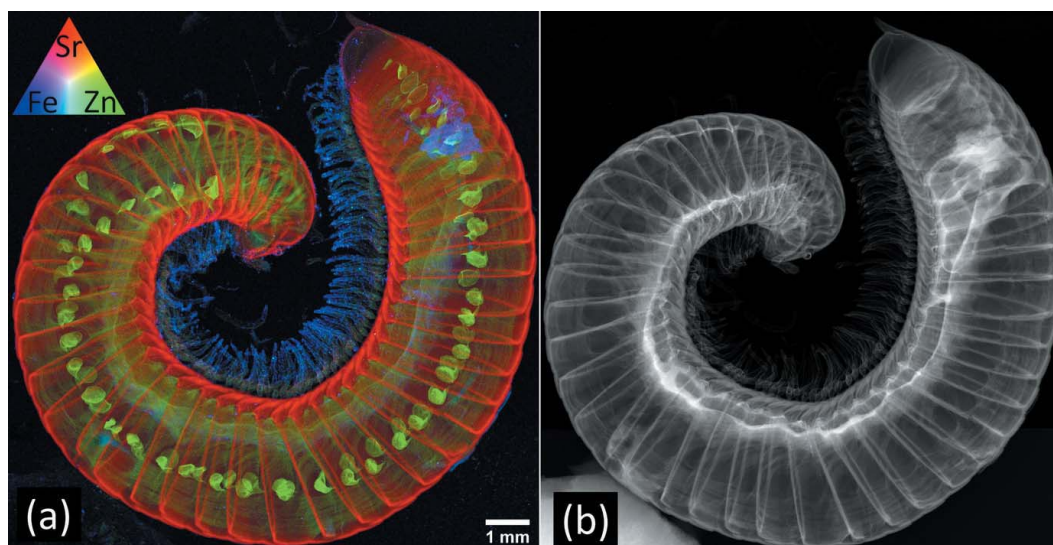
Figure 2
(*a*) Three-element false-colour composite elemental map of the Portuguese millipede (*Ommatoiulus moreleti*) measured with the Maia 384 detector array on XFM. The scan parameters are 5 µm × 5 µm pixel size, 1 ms dwell (5 mm s^{-1} scan velocity) and 2 h scan time. The zinc-rich sac-shaped ozadenes (stink glands) are present on the lateral side of most of the trunk segments. (*b*) The corresponding Compton scatter map highlights the overall morphology.

is then followed by higher-resolution analysis of regions of interest. Fast scanning is advantageous for 'needle in a haystack' measurements where large areas are scanned to find small particles, such as finding trace gold grains in the leaves of eucalyptus trees, which uptake gold grains in the soil through their root system (Lintern *et al.*, 2013).

7.2. XANES imaging

X-ray absorption near-edge structure (XANES) spectroscopy provides information on the structural and electronic properties of matter (Henderson *et al.*, 2014). Elemental mapping as a function of the incident energy across an element's absorption edge, known as XANES imaging or chemical state imaging, is a powerful tool to understand the elemental chemistry of heterogeneous samples (Etschmann *et al.*, 2014; Boesenberg *et al.*, 2018; Monico *et al.*, 2015). Here the absorption edge is studied with fluorescence yield detection, and the complete data set is often called a XANES stack. A benefit of 2D XANES imaging versus traditional single-point XANES is that it can give an improved chemical perspective of a heterogeneous specimen, since the area scanned is much larger than the probe size. In point XANES, elemental 'hotspots' are often the focus of attention, which may not necessarily be indicative of the true nature of the sample. Potential drifts of the sample or beam are readily identified and corrected in 2D XANES stacks because the movement is easily observed in the stack image sequence and, if present, can be aligned using fluorescence signals from spectator elements.

As implemented on XFM, a XANES stack begins at the top energy working down, the reason being to avoid the undulator backlash correction. At the completion of each 2D map, the incident energy is changed, the 2D map is repeated over the same area, and the process is repeated for a predefined number of energies, typically ranging from 60 to over 200. Depending on the area size and number of energies chosen, 2D XANES stacks take from 1.5 h, with 3 to 4 h commonplace. The time taken between the collection of each map in the XANES stack is currently about 21 s (thus mapping 100 energies = 35 min of overhead), which mainly comes from control overheads for detector setup and repopulating the scan parameters for motion control. We aim to reduce the current inter-scan time overhead to around 10 s, which is the present minimum required to allow controls handshaking after each scan and each change of energy.

Line XANES is a spatially resolved method of obtaining XANES in one dimension. Its advantage is that it is much quicker than 2D XANES imaging. As implemented on XFM, it is a horizontal traverse across the same line (*i.e.* Y is fixed) with the beam energy changing at each end of the line. Line XANES is particularly useful for the analysis of reference standards with a microfocus beam (Jones *et al.*, 2020). When the reference standards are powders, spatially resolved line XANES can permit the exclusion from the analysis of large particles that suffer from over-absorption. Depending on the line traverse time and the number of energies selected, line
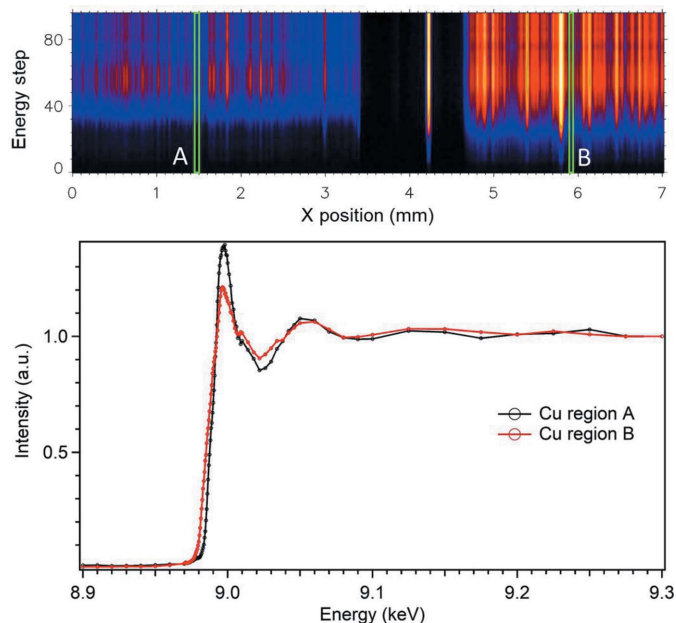

Figure 3
(Top) A line XANES example, showing the Cu K-edge line XANES of two powder reference samples on polyimide tape. (Bottom) Cu XANES traces extracted from the two highlighted regions labelled A (copper phosphate) and B (copper sulfide). Scan parameters: 95 energies, 7 mm wide transect, 10 μm pixel size, 10 ms dwell per pixel (1 mm s^{-1} scan velocity), 13.6 min total scan time.

XANES stacks take approximately 5–25 min. The collection of line XANES does not suffer from the above-mentioned time overheads between energies that 2D XANES mapping does. An example of line XANES at the copper K edge is shown in Fig. 3, recorded in under 14 min with 95 energies over a 7 mm wide transect.

7.3. XRF tomography

XRF tomography is capable of providing 3D structural visualization of trace metal distributions (de Jonge & Vogt, 2010). Naïve XRF tomography is optimal with a small specimen size and/or low-Z matrix to minimize 'self-absorption' of the emitted fluorescence, particularly of light elements; more sophisticated reconstruction algorithms are required when self-absorption effects are non-negligible (Di *et al.*, 2017). To enable tomographic measurements, a rotation stage is mounted via the standard specimen kinematic mount of the XYZ scanning stage stack. A pair of manual X–Z centring stages mounted atop the rotation stage, combined with the ethernet visualization cameras, permit easy centring of specimens. A Newport M-BK-1A with a 50 mm 'stick' of either 4 mm diameter Al or 2 mm diameter carbon fibre is used as a kinematic mount for the tomography specimens. The Al sticks can be relatively easily machined to accommodate a range of specimens.

Computed tomography (CT) reconstructions are greatly simplified when the rotation axis is orthogonal to the beam path, but reflection from the vertically focusing KB mirror directs the beam upwards at an angle of 6 mrad (twice the

mirror angle). In order to bring the rotation axis to a right angle to this beam, the entire optical table that supports the KB microprobe instrument is tilted to an angle of 6 mrad relative to the unfocused beam, and the vertical KB mirror pitch is tilted to −3 mrad relative to the table. This arrangement keeps the focused beam parallel to the table, and is also convenient for occasions when objects need to be moved around on the table. The angular range of the table is from −3 mrad to 9 mrad. The tilting table uses crossed flexure hinges at each end to maintain stiffness; this design was informed with help from the engineers at ALBA for a table used on the XALOC beamline (Juanhuix et al., 2014).

Thanks to its relatively quick acquisition time, single-slice computed tomography is a prevalent tomographic scanning mode on XFM. An alternative method for investigating trace elemental distributions within a specimen uses confocal optics. The beamline has a polycapillary optic (XOS) that can be mounted to the single-element Vortex detector for XRF confocal measurements. The confocal optic restricts the volumetric field of view of the detector, thus providing depth-specific analysis (Kanngießer et al., 2012). A combined CT–confocal investigation of a plant root is shown in Fig. 4 (van der Ent et al., 2018); from an initial 2D map of the root [Fig. 4(a)] a single plane of interest was identified and a single-slice tomography data set acquired using the Maia detector

Figure 4
(a) A 2D overview scan of a freeze-dried *Senecio coronatus* (Asteraceae) root acquired in 5.7 min, which allowed identification of a plane for tomographic investigation. (b) A tomographic sinogram with an estimated resolution of 5 μm, acquired in 10 min. (c) A 'virtual slice' reconstructed from the sinogram, showing the Ni and Compton scatter data of the root. (d) A confocal mapping of a small part of the root (70 × 50 pixels, each 20 × 20 μm) acquired with a polycapillary optic in 52 min. Figure reproduced with permission from van der Ent et al. (2018), copyright John Wiley and Sons.

[Fig. 4(b)], from which the Ni and scatter sinograms were reconstructed [Fig. 4(c)]. Careful accounting of the measurement positions and pre-characterization of the confocal optic alignment enabled rotation and translation of the specimen to bring any portion of the specimen to the confocal volume, located at the intersection of the beam and the focus of the confocal optic. The measurement sequence depicted here was acquired with the aim of developing a fast and efficient path to confocal or volumetric XANES measurements, but in this instance the low concentration of Ni in the root, combined with the low overall efficiency of the confocal optic, prevented acquisition of a statistically relevant XANES spectrum. Shown in Fig. 4(d) is a confocal map of the root, which is in broad agreement with the CT reconstruction; differences are due to the size of the confocal focus. However, the confocal measurement of a much smaller part of the root required around 52 min for a 20 μm × 20 μm pixel size, whereas the CT measurement was recorded in 10 min with an estimated resolution of 5 μm.

With fast single-slice tomography relatively routine, we have also added the dimension of varying energy to realize XANES slice tomography, which has been used to investigate Cu speciation in freeze-dried *Drosophila melanogaster* (James et al., 2016).

Scanning CT was achieved using a traverse-and-rotate addressing sequence. However, the narrow specimen dimensions required for first-generation fluorescence tomography mean that the traverse is very short, and even a small turn-around overhead can be prohibitive for these measurements. Investigating methods to overcome this limitation, we have developed spiral scanning XRF computed tomography. With the spiral scanning trajectory the specimen is rotated continuously while simultaneously undergoing a slow traverse of one resolution element per rotation. This approach yields some advantages and simplifications of the motion providing absolutely minimized motion overheads (de Jonge et al., 2017). The spiral scanning technique, however, requires excellent rotational motion control, such as repeatable radial eccentricity and negligible axial motion errors, which has prompted our recent acquisition of an LAB Motion Systems RT075S air-bearing rotation stage. The rotation stage has a resolution of 0.00152° and a maximum speed of 300 rpm.

7.4. Scanning transmission X-ray microscopy (STXM)

STXM yields complete knowledge of the complex-valued optical transmittance of the sample, or the object function. The object function contains the projection of the refractive index, $n = 1 - \delta a + i\beta$, where the real part δ describes the phase and the imaginary part β describes absorption. An EIGER2 X detector (http://www.dectris.com) records the intensity of the beam 4 m downstream of the sample. The EIGER2 produces 1 Mpixel images at up to 2250 Hz, triggered at each point in a scan to produce an ensemble of frames whose exposure commencement is exactly registered with pixel transitions of the sample scanning stages. STXM images therefore have the same pixel size as XRF images.
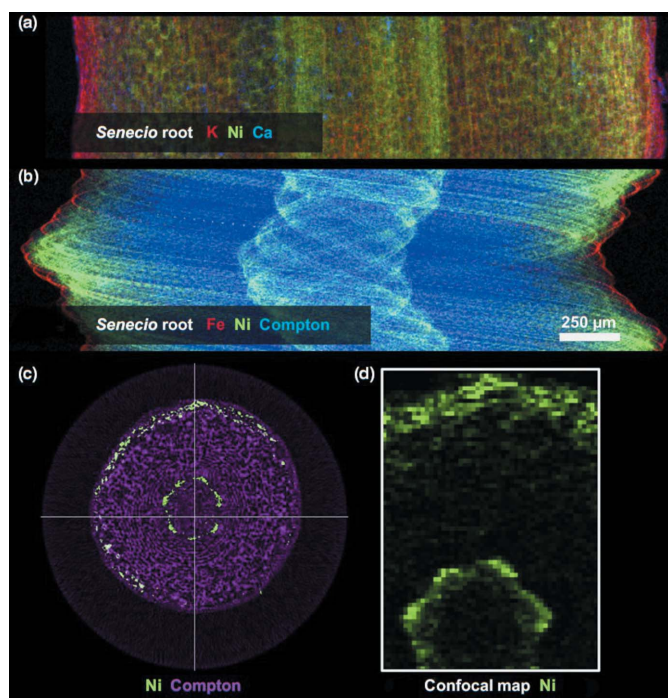
Each EIGER2 frame yields a single pixel in several STXM images with different contrast mechanisms: transmission, differential phase contrast (DPC) and darkfield. The transmission image is proportional to β and is obtained by integrating the whole frame. DPC images are proportional to the gradient of the phase, and are calculated by converting the displacement of the intensity profile into refraction angles in the horizontal and vertical directions (de Jonge *et al.*, 2008; Thibault *et al.*, 2009; Menzel *et al.*, 2010). The integrated phase is proportional to δ. Darkfield intensity integrated outside of the direct beam quantifies the scattering from sub-resolution features within the beam. The scattering can also be interrogated as a function of momentum transfer in a manner similar to scanning small-angle X-ray scattering (SAXS) (Bunk *et al.*, 2009).

7.5. Ptychography

Ptychography, or scanning X-ray diffraction microscopy (SXDM), provides complex super-resolution images of the object function and the beam from coherent diffraction patterns measured from overlapping regions of a sample (Thibault *et al.*, 2008). The optimum data collection for ptychography requires a coherent incident beam, scan pixels smaller than the beam size to ensure sufficient overlap (Bunk *et al.*, 2008), and an X-ray detector capable of simultaneously recording both single photons and the direct beam. The achievable spatial resolution is diffraction-limited, dependent on the X-ray wavelength and the detection solid angle. Although the resolution is in principle wavelength-limited, in practice the resolution is limited by the precision of the intensity and position measurements (Thibault & Menzel, 2013) and radiation damage to the sample (Howells *et al.*, 2009).

Experimental conditions for ptychography on XFM were designed through consideration of the phase-space filling at the location of each optical aperture along the beamline: thousands of coherent modes at the source were reduced by spatial filtering to a single coherent mode after the secondary source (de Jonge, 2018). The coherent theoretically modelled 'monomodal' beam is extracted by closing the white-beam slits to 0.1 mm × 0.1 mm and the SSA from several to tens of micrometres wide, reducing the flux to about 4×10^8 photons s^{-1} prior to focusing by the KB mirrors. As expected theoretically, the focusing performance of the KB mirrors is optimized with coherent illumination. The coherent beam size is approximately 350 nm × 550 nm, and X-ray fluorescence measurements obtained simultaneously with ptychography data show much higher spatial resolution than mapping with the incoherent full-intensity beam.

Ptychography scans typically use a 100 nm pixel size and scan velocities in the μm s^{-1} range, resulting in tens of milliseconds dwell per EIGER2 frame. Zooming in on an object region-of-interest spanning 30 μm × 30 μm may take up to half an hour and result in a data set containing 10^5 diffraction patterns. An automated data analysis pipeline pre-processes the EIGER2 data for ptychographic reconstructions using a dedicated cluster of computer nodes. As the resolution in ptychography is diffraction- and dose-limited, the reconstructed image pixel size is chosen in accordance with the scattering strength of the sample. A typical case would reconstruct 20 nm image pixels using the data contained in a detector region-of-interest of 256 pixels × 256 pixels surrounding the direct beam. A reconstruction of an 11 μm × 10 μm area of an integrated circuit serving as a test sample is shown in Fig. 5, comparing XRF imaging in Fig. 5(*a*) with STXM imaging in Figs. 5(*b*)–5(*d*) and ptychographic imaging in Figs. 5(*e*) and 5(*f*), which were all measured simultaneously. In comparison with the XRF measurement which directly determines the different elements in the sample, the ptychographic reconstructions yield much higher spatial resolution resolving the finest features, such as the small tungsten plugs. Simultaneous ptychography and elemental imaging of nematodes has also been demonstrated on XFM, yielding 'super-resolution' morphological information with elemental distribution (Jones, Phillips *et al.*, 2019).
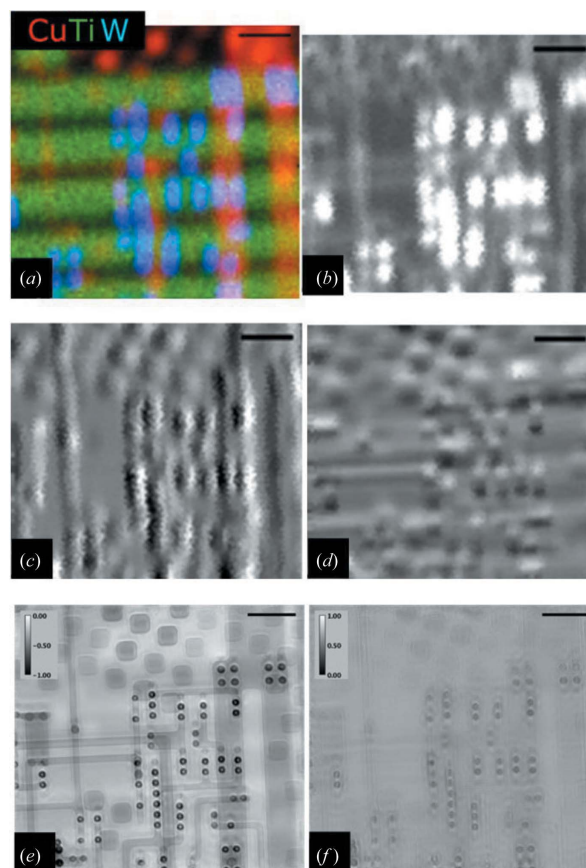

Figure 5
High-resolution images of an integrated circuit. (*a*) RGB image of the XRF maps of copper (red), titanium (green) and tungsten (blue) recorded with a coherent beam of about 500 nm FWHM. (*b*)–(*d*) Scanning transmission X-ray microscopy (STXM) images showing (*b*) the darkfield scattering intensity integrated outside the transmitted beam, (*c*) the differential phase-contrast (DPC) in the horizontal (*X*) direction and (*d*) the DPC in the vertical (*Y*) direction. (*e*), (*f*) Ptychographic 'super-resolution' reconstructions from the STXM data, showing (*e*) the phase (in radians) and (*f*) the transmission (normalized to 1) with a pixel size of 38 nm. All scale bars are 2 μm.

7.6. Other

The potential of using energy-dispersive X-ray area detectors for materials characterization was investigated with the Maia detector. The large annular geometry of Maia has permitted simultaneous measurement of XRF and diffraction grain mapping of a polycrystalline foil, simultaneously measuring X-ray fluorescence and diffraction to determine grain orientation and estimate lattice strain (Kirkwood *et al.*, 2017).

Depth sensitivity is possible due to the large size of the Maia detector array. It provides a wide range of takeoff angles at the sample surface, with the angle between the sample normal and ray to masked detector centre varying between 13.9° and 52.6°. This makes the outer detectors much more sensitive to self-absorption for X-rays from a particle at depth in a sample than the inner detectors. Such a difference can be utilized to provide an imaging contrast based on particle depth and also a quantitative measure of depth for discrete identified particles. An example is depth mapping of Pt particles in geological sections (Ryan *et al.*, 2013).

8. Data analysis

Users of XFM have access to the Australian Synchrotron Computing Infrastructure (ASCI) for their data analysis during and after their beam time. ASCI is a high-performance computing platform to allow researchers who have collected data at the Australian Synchrotron to process and visualize their data. The ASCI interface is easily accessible with a web browser. Users are able to download their data through SFTP clients or `rsync`.

GeoPIXE software is installed on ASCI and is used for all XRF analysis on XFM (Ryan *et al.*, 1990). With *GeoPIXE*, full spectral XRF data are deconvoluted into elemental concentration maps using a matrix transform method called dynamic analysis (DA) (Ryan, 2000). The DA method provides a linear least-squares fit result at real-time processing speed. The model includes all excited X-ray lines, pile-up peaks, escape peaks, background terms, and elastic and inelastic scattering peaks. A fit of a specimen's XRF spectrum, including parameters such as the sample characteristics, *i.e.* the sample matrix composition and thickness, is used to create the DA transform matrix, which can be applied to similar scans having the same attributes. The method has been extended to 2D XANES imaging by shifting the centroids of the elastic and inelastic peaks to track the changing beam energy. The full nonlinear fit is executed on the XRF spectrum at the top beam energy for the XANES scan, in which the shape of the background and the inelastic scattering distributions are determined. A series of DA matrices are generated as the beam energy is reduced, with the elastic and inelastic scatter peaks shifted to track the change in beam energy. The value of this approach is the acquisition of XANES spectra for each *XY* position with subtraction of contributions due to scattering, background and other elements. For 1D or line XANES, a fixed incident energy is assumed.

The beamline has a collection of standard reference metal concentration foils (Micromatter) that are scanned routinely for flux quantitation to ultimately provide quantitative sample concentrations. The sample matrix and sample thickness must be well characterized for reliable quantitation.

Starting in 2020, user data will be retained on Australian Synchrotron storage for one year for merit-based experiments on XFM, unless an extension has been requested and approved. After the retention period, data may be deleted at any time. Data may be deposited in a public access archive at the discretion of the Australian Synchrotron.

9. Future upgrades

A double multilayer monochromator (DMM) has been funded and is designed to effectively transmit the entire energy width of the in-vacuum undulator (IVU) source with a bandpass of $\sim 10^{-2}$, providing an order of magnitude more flux than the DCM. To cover the energy range, the materials planned for the DMM stripes are Mo/B_4C (10–20 keV) and W/B_4C (15–30 keV).

For improved detection efficiency at higher energies, *e.g.* at the Cd *K* edge, we propose to acquire a thicker sensor silicon drift detector or high-purity germanium (HPGe) detector. In cases where escape peaks pose a problem with silicon sensors, *e.g.* the detection of phosphorus in a calcium-rich matrix, a benefit of the HPGe detector is its different escape peak energy, thus providing a complementary function relative to silicon.

For milliprobe operations, a sample protection system is planned using compact Micro-Epsilon optoNCDT 1320 laser triangulation displacement sensors. The sensors will measure the distance from the Maia detector to the sample and will interlock the motion control system if the sample is too close. The laser sensor streams the measured distances, so topographical maps of sample surfaces are possible.

Environmental control of temperature and relative humidity (RH) in the XFM endstation is planned, which can be important for sensitive samples. The nominal temperature of the beamline endstation is 26°C. Temperature control will be useful for experiments with temperature-sensitive components, and for maintaining spatial/position stability. Earlier in our operation, the RH was relatively stable at $55 \pm 5\%$ (Howard *et al.*, 2012); now it varies by approximately $\pm 25\%$. The benefits of RH control are that lower RH will reduce icing for measurements requiring the Cryostream, and stable RH will benefit wooden objects such as panel paintings that are sensitive to RH extremes, which can potentially cause deformations in the wood.

An offline sample pre-alignment system with co-registered coordinates is planned. The system will allow users to obtain initial scan coordinates for samples before and during their experiment. Depending on the nature of the samples, this could potentially save several hours of beam time. This system also enables developmental work on the scanning stages without experimental interruption.

1456   Daryl L. Howard *et al.* • The XFM beamline at the Australian Synchrotron   *J. Synchrotron Rad.* (2020). **27**, 1447–1458

electronic reprint

For experiments requiring cryocooling, liquid nitrogen currently takes 8 h to install. We aim to have a dedicated liquid nitrogen supply within the XFM endstation to make this available within 30 min.

We are working towards a limited mail-in program where users can post samples to the beamline, and beamline staff can mount and scan them. Users will be able to analyse the data remotely, and communicate further experimental decisions in collaboration with the beamline staff.

10. Facility access

The Australian Synchrotron makes its beamlines available to the research community and industry through peer-reviewed, collaborative and commercial arrangements. The Australian Synchrotron is free of charge for all researchers who are publishing results in the open literature and beam time is allocated through the peer-review application process. There is a fee structure for commercial users.

11. Conclusions

The recent and planned upgrades on XFM should allow the user community to access state-of-the-art research facilities for years to come. We also look forward to the new build of beamlines at the Australian Synchrotron under the BRIGHT project, such as the X-ray Fluorescence Nanoprobe, Medium-Energy X-ray Absorption Spectroscopy (MEX) beamline and the Micro-Computed Tomography (MCT) beamline, which will complement XFM's capabilities (https://www.ansto.gov.au/research/facilities/australian-synchrotron/project-bright).

APPENDIX *A*
Instrument energy resolution

In a simplified approach for an instrument energy-resolution calculation, two main components contribute to broadening of an edge step, specifically the intrinsic absorption edge width due to the natural width of the core level (Krause & Oliver, 1979) and the instrumental resolution ΔE_i due to beamline optics. In this approach, each contribution can be considered as having a Gaussian distribution. The resulting overall resolution is given by $\Delta E^2 = [\Gamma^2 + \Delta E_i^2]^{1/2}$ (Poswal *et al.*, 2016), where ΔE is determined from the FWHM of the first derivative of the *K*-edge absorption spectrum, and Γ is the natural line width The instrumental resolution ΔE_i depends on the inherent resolution of the monochromator reflection and the beam divergence. We present data for Se and Cu to determine the instrumental resolution on XFM for the Si(111) crystals.

The first-order derivative of an Se *K*-edge XANES spectrum is shown in Fig. 6, and the value of ΔE determined from the FWHM of the first derivative is 4.5 eV. Using the natural width of the core level Γ of the Se *K* edge as 2.33 eV (Krause & Oliver, 1979), we obtain an instrumental resolution ΔE_i of 3.9 eV at the Se *K*-edge energy of 12 658 eV, corresponding to $\Delta E_i/E \simeq 3.1 \times 10^{-4}$. Likewise for Cu, we observe $\Delta E = 3.2$ eV, and using $\Gamma = 1.55$ for Cu, we obtain $\Delta E_i = 2.8$ eV at
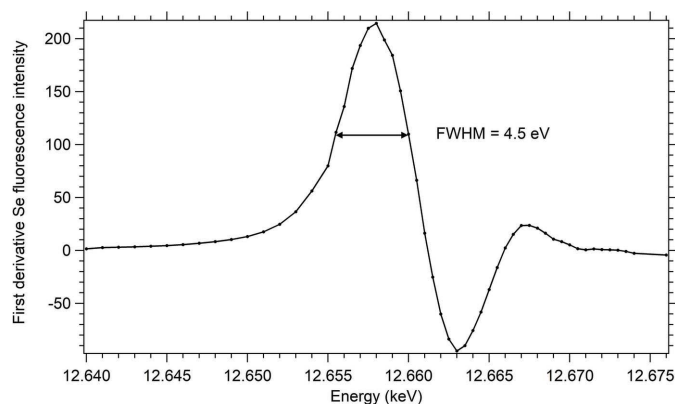

Figure 6
First-order derivative of Se *K*-edge XANES recorded from an XRF standard foil (Micromatter) in fluorescence yield.

the Cu *K*-edge energy of 8979 eV, again corresponding to $\Delta E_i/E \simeq 3.1 \times 10^{-4}$. This is in good agreement with $\Delta E_i/E \simeq 2.8 \times 10^{-4}$ determined by Liu *et al.* (2017) in their study of the As *K* edge, in which the monochromator was considered the limiting parameter. Although $\Delta E_i/E$ for XFM is approximately double that of beamlines designed for spectroscopy, we have found very good agreement between, for example, Cr and As *K*-edge XANES collected on XFM and on other beamlines with identical samples (Monico *et al.*, 2015; Liu *et al.*, 2017).

References

Afshar, N., Howard, D., Paterson, D., Starritt, A. C. & de Jonge, M. D. (2017). *International Conference on Accelerator and Large Experimental Control Systems*, 8–13 October 2017, Barcelona, Spain. Volume edited by V. R. W. Schaa, I. Costa, D. Fernández & O. Matilla, WEBPL07. http://accelconf.web.cern.ch/icalepcs2017/talks/webpl07_talk.pdf. Geneva: JACoW.

Bissardon, C., Reymond, S., Salomé, M., André, L., Bayat, S., Cloetens, P. & Bohic, S. (2019). *J. Visual Exp.* e60461.

Blamey, F. P. C., Paterson, D. J., Walsh, A., Afshar, N., McKenna, B. A., Cheng, M., Tang, C., Horst, W. J., Menzies, N. W. & Kopittke, P. M. (2018). *Environ. Exp. Bot.* **156**, 151–160.

Boesenberg, U., Ryan, C. G., Kirkham, R., Jahn, A., Madsen, A., Moorhead, G., Falkenberg, G. & Garrevoet, J. (2018). *J. Synchrotron Rad.* **25**, 892–898.

Boldeman, J. & Einfeld, D. (2004). *Nucl. Instrum. Methods Phys. Res. A*, **521**, 306–317.

Bunk, O., Bech, M., Jensen, T. H., Feidenhans'l, R., Binderup, T., Menzel, A. & Pfeiffer, F. (2009). *New J. Phys.* **11**, 123016.

Bunk, O., Dierolf, M., Kynde, S., Johnson, I., Marti, O. & Pfeiffer, F. (2008). *Ultramicroscopy*, **108**, 481–487.

Carter, E., Rayner, B., McLeod, A., Wu, L., Marshall, C., Levina, A., Aitken, J., Witting, P., Lai, B., Cai, Z., Vogt, S., Lee, Y.-C., Chen, C.-I., Tobin, M., Harris, H. & Lay, P. (2010). *Mol. Biosyst.* **6**, 1316–1322.

Di, Z. W., Chen, S., Hong, Y. P., Jacobsen, C., Leyffer, S. & Wild, S. M. (2017). *Opt. Express*, **25**, 13107–13124.

Divitcos, J., De Jonge, M., Howard, D. & McKinlay, J. (2017). *Mechanical Engineering Design of Synchrotron Radiation Equipment and Instrumentation Conference*, 11–16 September 2016, Barcelona, Spain, Volume edited by V. R. W. Schaa, pp. 93–95. Geneva: JACoW.

Donner, E., de Jonge, M., Kopittke, P. M. & Lombi, E. (2013). *Methods Mol. Biol.* **953**, 143–159.

Eng, P. J., Newville, M., Rivers, M. L. & Sutton, S. R. (1998). *Proc. SPIE*, **3449**, 145–156.

Ent, A. van der, Przybyłowicz, W., de Jonge, M., Harris, H., Ryan, C., Tylko, G., Paterson, D., Barnabas, A., Kopittke, P. M. & Mesjasz-Przybyłowicz, J. (2018). *New Phytol.* **218**, 432–452.

Etschmann, B. E., Donner, E., Brugger, J., Howard, D. L., de Jonge, M. D., Paterson, D., Naidu, R., Scheckel, K. G., Ryan, C. G. & Lombi, E. (2014). *Environ. Chem.* **11**, 341–350.

Gei, V., Erskine, P., Harris, H., Echevarria, G., Mesjasz-Przybyłowicz, J., Barnabas, A., Przybyłowicz, W. & Ent, A. (2018). *Agromining: Farming for Metals*, edited by A. Van der Ent, G. Echevarria, A. Baker & J. Morel, pp. 117–133. Cham: Springer.

Henderson, G., de Groot, F. & Moulton, B. (2014). *Rev. Mineral. Geochem.* **78**, 75–138.

Howard, D. L., de Jonge, M. D., Lau, D., Hay, D., Varcoe-Cocks, M., Ryan, C. G., Kirkham, R., Moorhead, G., Paterson, D. & Thurrowgood, D. (2012). *Anal. Chem.* **84**, 3278–3286.

Howard, D. L., de Jonge, M. D., Paterson, D. & Thurrowgood, D. (2018). *Microsc. Microanal.* **24**, 488–489.

Howells, M. R., Beetz, T., Chapman, H. N., Cui, C., Holton, J. M., Jacobsen, C. J., Kirz, J., Lima, E., Marchesini, S., Miao, H., Sayre, D., Shapiro, D. A., Spence, J. C. H. & Starodub, D. (2009). *J. Electron Spectrosc. Relat. Phenom.* **170**, 4–12.

James, S. A., Burke, R., Howard, D. L., Spiers, K. M., Paterson, D. J., Murphy, S., Ramm, G., Kirkham, R., Ryan, C. G. & de Jonge, M. D. (2016). *Chem. Commun.* **52**, 11834–11837.

James, S. A., Feltis, B. N., de Jonge, M. D., Sridhar, M., Kimpton, J. A., Altissimo, M., Mayo, S., Zheng, C., Hastings, A., Howard, D. L., Paterson, D. J., Wright, P. F. A., Moorhead, G. F., Turney, T. W. & Fu, J. (2013). *ACS Nano*, **7**, 10621–10635.

Jones, M. W. M., Hare, D. J., James, S. A., de Jonge, M. D. & McColl, G. (2017). *Anal. Chem.* **89**, 12168–12175.

Jones, M. W. M., Kopittke, P. M., Casey, L., Reinhardt, J., Blamey, F. P. C. & van der Ent, A. (2019). *Ann. Bot.* **125**, 599–610.

Jones, M. W. M., Mallmann, G., Wykes, J. L., Knafelc, J., Bryan, S. E. & Howard, D. L. (2020). *J. Synchrotron Rad.* **27**, 207–211.

Jones, M. W. M., Phillips, N. W., Abbey, B., Hare, D. J., van Riessen, G. A., Vine, D. J., de Jonge, M. D. & McColl, G. (2019). *Chem. Commun.* **55**, 1052–1055.

Jonge, M. de (2018). Personal communication.

Jonge, M. D. de, Hornberger, B., Holzner, C., Legnini, D., Paterson, D., McNulty, I., Jacobsen, C. & Vogt, S. (2008). *Phys. Rev. Lett.* **100**, 163902.

Jonge, M. D. de, Kingston, A. M., Afshar, N., Garrevoet, J., Kirkham, R., Ruben, G., Myers, G. R., Latham, S. J., Howard, D. L., Paterson, D. J., Ryan, C. G. & McColl, G. (2017). *Opt. Express*, **25**, 23424–23436.

Jonge, M. D. de & Vogt, S. (2010). *Curr. Opin. Struct. Biol.* **20**, 606–614.

Juanhuix, J., Gil-Ortiz, F., Cuní, G., Colldelram, C., Nicolás, J., Lidón, J., Boter, E., Ruget, C., Ferrer, S. & Benach, J. (2014). *J. Synchrotron Rad.* **21**, 679–689.

Kanngießer, B., Malzer, W., Mantouvalou, I., Sokaras, D. & Karydas, A. G. (2012). *Appl. Phys. A*, **106**, 325–338.

Kirkham, R., Dunn, P. A., Kuczewski, A. J., Siddons, D. P., Dodanwela, R., Moorhead, G. F., Ryan, C. G., De Geronimo, G., Beuttenmuller, R., Pinelli, D., Pfeffer, M., Davey, P., Jensen, M., Paterson, D. J., de Jonge, M. D., Howard, D. L., Küsel, M., McKinlay, J., Garrett, R., Gentle, I., Nugent, K. & Wilkins, S. (2010). *AIP Conf. Proc.* **1234**, 240–243.

Kirkwood, H. J., de Jonge, M. D., Howard, D. L., Ryan, C. G., van Riessen, G., Hofmann, F., Rowles, M. R., Paradowska, A. M. & Abbey, B. (2017). *Powder Diffr.* **32**, S16–S21.

Krause, M. O. & Oliver, J. H. (1979). *J. Phys. Chem. Ref. Data*, **8**, 329–338.

Lai, B., Vogt, S. & Maser, J. (2007). *AIP Conf. Proc.* **879**, 1313–1316.

Lintern, M., Anand, R., Ryan, C. & Paterson, D. (2013). *Nat. Commun.* **4**, 2614.

Liu, W., Mei, Y., Etschmann, B., Brugger, J., Pearce, M., Ryan, C. G., Borg, S., Wykes, J., Kappen, P., Paterson, D., Boesenberg, U., Garrevoet, J., Moorhead, G. & Falkenberg, G. (2017). *Geochim. Cosmochim. Acta*, **196**, 144–159.

McColl, G., James, S. A., Mayo, S., Howard, D. L., Ryan, C. G., Kirkham, R., Moorhead, G. F., Paterson, D., de Jonge, M. D. & Bush, A. I. (2012). *PLoS One*, **7**, e32685.

Menzel, A., Kewish, C. M., Kraft, P., Henrich, B., Jefimovs, K., Vila-Comamala, J., David, C., Dierolf, M., Thibault, P., Pfeiffer, F. & Bunk, O. (2010). *Ultramicroscopy*, **110**, 1143–1147.

Monico, L., Janssens, K., Alfeld, M., Cotte, M., Vanmeert, F., Ryan, C. G., Falkenberg, G., Howard, D. L., Brunetti, B. G. & Miliani, C. (2015). *J. Anal. At. Spectrom.* **30**, 613–626.

Paterson, D., De Jonge, M. D., Howard, D. L., Lewis, W., McKinlay, J., Starritt, A., Kusel, M., Ryan, C. G., Kirkham, R., Moorhead, G. & Siddons, D. P. (2011). *AIP Conf. Proc.* **1365**, 219–222.

Paterson, D. J., Boldeman, J. W., Cohen, D. D. & Ryan, C. G. (2007). *AIP Conf. Proc.* **879**, 864–867.

Poswal, A. K., Agrawal, A., Poswal, H. K., Bhattacharyya, D., Jha, S. N. & Sahoo, N. K. (2016). *J. Synchrotron Rad.* **23**, 1518–1525.

Ryan, C. G. (2000). *Int. J. Imaging Syst. Technol.* **11**, 219–230.

Ryan, C. G., Cousens, D. R., Sie, S. H., Griffin, W. L., Suter, G. F. & Clayton, E. (1990). *Nucl. Instrum. Methods Phys. Res. B*, **47**, 55–71.

Ryan, C. G., Kirkham, R., de Jonge, M. D., Siddons, D. P., van der Ent, A., Pagés, A., Boesenberg, U., Kuczewski, A. J., Dunn, P., Jensen, M., Liu, W., Harris, H., Moorhead, G. F., Paterson, D. J., Howard, D. L., Afshar, N., Garrevoet, J., Spiers, K., Falkenberg, G., Woll, A. R., De Geronimo, G., Carini, G. A., James, S. A., Jones, M. W. M., Fisher, L. A. & Pearce, M. (2018). *Synchrotron Radiat. News*, **31**, 21–27.

Ryan, C. G., Siddons, D. P., Kirkham, R., Li, Z. Y., de Jonge, M. D., Paterson, D., Cleverley, J. S., Kuczewski, A., Dunn, P. A., Jensen, M., De Geronimo, G., Howard, D. L., Godel, B., Dyl, K. A., Fisher, L. A., Hough, R. H., Barnes, S. J., Bland, P. A., Moorhead, G., James, S. A., Spiers, K. M., Falkenberg, G., Boesenberg, U. & Wellenreuther, G. (2013). *Proc. SPIE*, **8851**, 88510Q.

Ryan, C. G., Siddons, D. P., Kirkham, R., Li, Z. Y., de Jonge, M. D., Paterson, D. J., Kuczewski, A., Howard, D. L., Dunn, P. A., Falkenberg, G., Boesenberg, U., De Geronimo, G., Fisher, L. A., Halfpenny, A., Lintern, M. J., Lombi, E., Dyl, K. A., Jensen, M., Moorhead, G. F., Cleverley, J. S., Hough, R. M., Godel, B., Barnes, S. J., James, S. A., Spiers, K. M., Alfeld, M., Wellenreuther, G., Vukmanovic, Z. & Borg, S. (2014). *J. Phys. Conf. Ser.* **499**, 012002.

Scoullar, P. A. B., McLean, C. C., Evans, R. J., Hamm, M. E. & Hamm, R. W. (2011). *AIP Conf. Proc.* **1412**, 270–277.

Sun, Y., Gleber, S.-C., Jacobsen, C., Kirz, J. & Vogt, S. (2015). *Ultramicroscopy*, **152**, 44–56.

Thibault, P., Dierolf, M., Kewish, C. M., Menzel, A., Bunk, O. & Pfeiffer, F. (2009). *Phys. Rev. A*, **80**, 043813.

Thibault, P., Dierolf, M., Menzel, A., Bunk, O., David, C. & Pfeiffer, F. (2008). *Science*, **321**, 379–382.

Thibault, P. & Menzel, A. (2013). *Nature*, **494**, 68–71.

Thurrowgood, D., Paterson, D., de Jonge, M. D., Kirkham, R., Thurrowgood, S. & Howard, D. L. (2016). *Sci. Rep.* **6**, 29594.